

2D MATERIALS

A quantum ruler for orbital magnetism in moiré quantum matter

M. R. Slot^{1,2†}, Y. Maximenko^{1,3†}, P. M. Haney¹, S. Kim^{1,4}, D. T. Walkup¹, E. Strelcov^{1,3}, Son T. Le¹, E. M. Shih^{1,3}, D. Yildiz^{1,4}, S. R. Blankenship¹, K. Watanabe⁵, T. Taniguchi⁶, Y. Barlas⁷, N. B. Zhitenev¹, F. Ghahari^{8*}, J. A. Stroscio^{1*}

For almost a century, magnetic oscillations have been a powerful “quantum ruler” for measuring Fermi surface topology. In this study, we used Landau-level spectroscopy to unravel the energy-resolved valley-contrasting orbital magnetism and large orbital magnetic susceptibility that contribute to the energies of Landau levels of twisted double-bilayer graphene. These orbital magnetism effects led to substantial deviations from the standard Onsager relation, which manifested as a breakdown in scaling of Landau-level orbits. These substantial magnetic responses emerged from the nontrivial quantum geometry of the electronic structure and the large length scale of the moiré lattice potential. Going beyond traditional measurements, Landau-level spectroscopy performed with a scanning tunneling microscope offers a complete quantum ruler that resolves the full energy dependence of orbital magnetic properties in moiré quantum matter.

Moiré quantum matter (MQM) systems (1) consist of stacked and twisted layers of van der Waals materials and have emerged as versatile condensed-matter quantum simulators (2). The twist angle, choice of material, number of layers, and the application of electric and magnetic fields provide a vast arena for realizing quantum phases that result from the interplay between electron correlations and topology. The discovery of flat electronic bands that host superconductivity and correlated insulating states in magic-angle twisted bilayer graphene (MATBG) inspired rapid exploration of the parameter space (3–5). The most recent endeavors have focused on heterostructures of three, four, and five layers of alternating twisted graphene monolayers (6–11).

The moiré systems of MATBG and related heterostructures support topological bands with nonzero Chern number (4, 12), which is derived from the Berry curvature of the Bloch wave functions (13). Berry curvature is intimately related to orbital magnetization, and indeed, previous work on MATBG and related systems has observed orbital magnetic order, valley Hall,

and quantum anomalous Hall effects (14–16). Berry curvature and the related quantum metric also provide significant contributions to the orbital magnetic susceptibility (17, 18). The valley-contrasting orbital magnetism and orbital magnetic susceptibility play a central role in the material response to applied magnetic fields. Landau-level (LL) spectroscopy is a well-established tool to experimentally deduce the zero-field properties of the band structure, and in this work, we expand its application to extracting higher-order magnetic response functions.

Semiclassically, LLs are described by the Onsager relation, relating the extremal cross-sectional area of the Fermi surface to the period of oscillations in the de Haas–van Alphen effect (19). The orbital magnetism and orbital magnetic susceptibility give rise to energy-dependent first- and second-order corrections with magnetic field in the Onsager relation (20), which was recently formulated as a general expansion in higher-order response functions (21). To determine these effects and their full energy dependence, high-resolution measurements of the LLs in the electronic bands are required: a “quantum ruler” probing the evolution of LLs at all energies as a function of displacement field and magnetic field.

In this work, we used LL measurements as a quantum ruler for twisted double-bilayer graphene (TDBG) to quantitatively determine the tunable electronic structure, energy-dependent valley-contrasting orbital magnetism, and orbital magnetic susceptibility. TDBG is MQM with highly reconfigurable bands; the Bernal bilayer constituents have an electrostatically tunable band structure in themselves (22–37). Flat bands exist over a wide range of small twist angles (θ), from about 0.8° to 1.5° . Previous transport and scanning tunneling micro-

scopy (STM) measurements have focused on correlated states, which form at various partial fillings (22–30), or density wave states at larger twist angles of $\theta \approx 2.4^\circ$ (31). Our intermediate twist angle of 1.74° gives rise to moiré minibands that are narrow but not extremely flat. This slightly wider bandwidth allows LLs to be resolved over the entire band structure, which has not been observed in previous local probe measurements (29).

Tuning the electronic structure of TDBG

Figure 1A shows the simulated band structure of TDBG at $\theta = 1.75^\circ$ with the Bistritzer–MacDonald (BM) continuum model (3). The moiré periodic potential leads to narrow moiré minibands, composed of two low-energy bands—the valence V1 and conduction C1 bands—and higher remote energy bands—V2 and C2. The narrow bands V1 and C1 have a bandwidth of about 50 meV and are isolated from other bands (Fig. 1B). The TDBG system displays a large tunability in its electronic structure (12, 32–39). A perpendicular electric field induces a potential difference between the layers of TDBG, drastically altering the V1 band structure. The V1 band is relatively flat at zero displacement field (D) (Fig. 1B) and develops pronounced electron and hole pockets at $D \neq 0$ (Fig. 1C and fig. S8). In the next section, we first describe the measurement of this band structure evolution under a displacement field.

Measurements were performed in a custom-built dilution refrigerator-based scanning probe system operating at 10 mK (40, 41). Figure 1D shows the STM topograph of the TDBG sample used in this study (fig. S1). The measured moiré periodicity of $\lambda = (8.1 \pm 0.1)$ nm corresponds to a twist angle of $\theta = (1.74^\circ \pm 0.02^\circ)$, and the local heterostrain was found to be $<0.1\%$, as determined from atomically resolved spatial measurements (42). Scanning tunneling spectroscopy (STS) measures the differential tunneling conductance (dI/dV) signal, which is proportional to the local density of states (LDOS) (43). For TDBG, the measured dI/dV reflects the LDOS of the topmost layer of the four-layer system. The finite tip potential leads to a fixed top gate V_T , determined by the contact-potential difference between probe and sample. Varying the back-gate voltage V_G simultaneously tunes the displacement field D and the carrier density n following $D \propto C_G V_G - C_T V_T$ and $n \propto C_G V_G + C_T V_T$, where C_G and V_G are the back-gate capacitance and voltage, and C_T and V_T are tip capacitance and potential, respectively (42). We mapped the differential tunneling conductance as a function of sample bias V_B , the displacement field D , carrier density n , and magnetic field B . Figure 1E shows the experimental LDOS map at $B = 0$ T. The low-energy bands V1 and C1 and remote bands V2 and C2 and their

¹Physical Measurement Laboratory, National Institute of Standards and Technology, Gaithersburg, MD 20899, USA.

²Department of Physics, Georgetown University, Washington, DC 20007, USA. ³Department of Chemistry and Biochemistry, University of Maryland, College Park, MD 20742, USA.

⁴Joint Quantum Institute, Department of Physics, University of Maryland, College Park, MD 20742, USA.

⁵Research Center for Functional Materials, National Institute for Materials Science, 1-1 Namiki, Tsukuba, Ibaraki 305-0044, Japan. ⁶International Center for Materials Nanoarchitectonics, National Institute for Materials Science, 1-1 Namiki, Tsukuba, Ibaraki 305-0044, Japan. ⁷Department of Physics, University of Nevada, Reno, NV 89557, USA.

⁸Department of Physics and Astronomy, George Mason University, Fairfax, VA 22030, USA.

*Corresponding author. Email: fghahari@gmu.edu (F.G.); joseph.stroscio@nist.gov (J.A.S.)

†These authors contributed equally to this work.

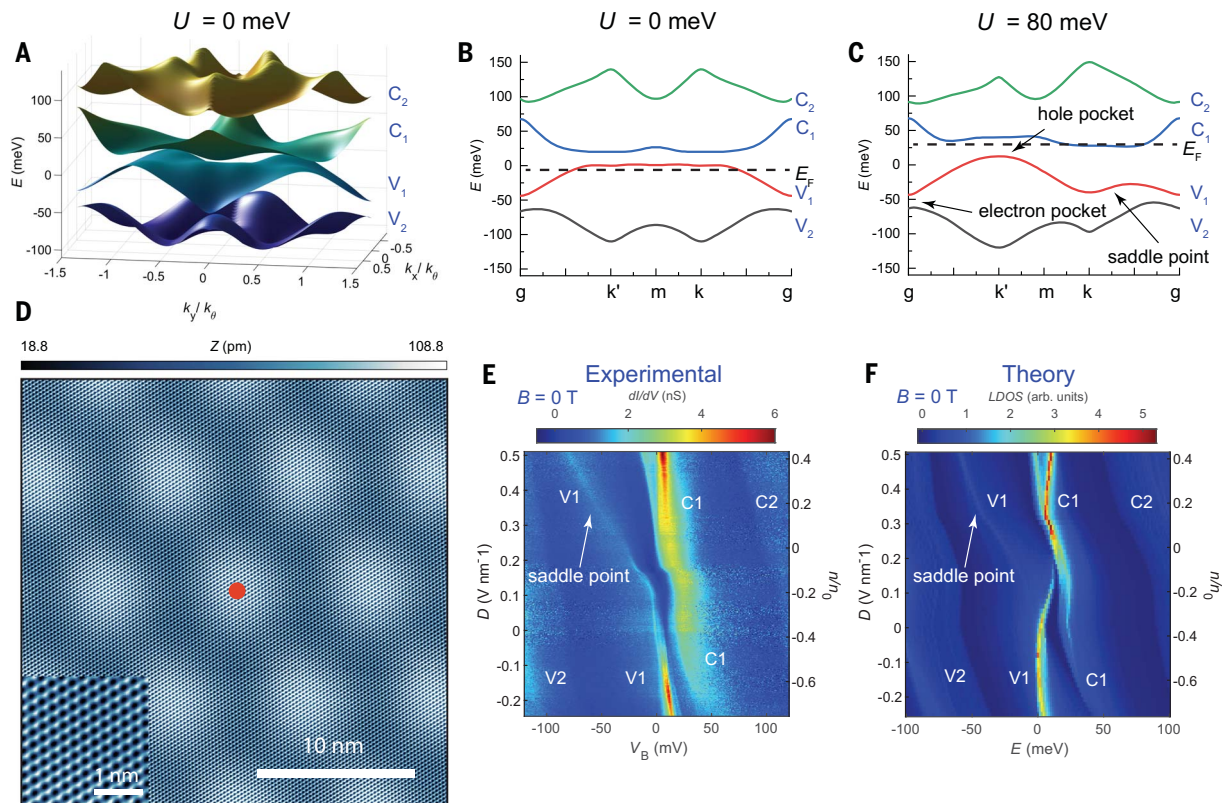


Fig. 1. Tuning the narrow electronic bands in TDBG with displacement field at $\theta = 1.75^\circ$. (A) Energy-band structure of TDBG showing the four low-energy bands computed by using a continuum model with interlayer potential $U = 0$ meV and $\theta = 1.75^\circ$. Line cuts from the energy bands in (A) along Bloch wave vector $k_x = 0$ for (B) $U = 0$ meV and (C) $U = 80$ meV. A dashed horizontal line indicates the position of the Fermi level (E_F), which moves through the bands as the displacement field and carrier density are varied. The x-axis labels (g, k', m, and k) denote high-symmetry points in the mini-Brillouin zone. (D) STM topographic image of the TDBG moiré pattern, with moiré

wavelength $\lambda = (8.1 \pm 0.1)$ nm. (Inset) A magnified portion of the image showing the atomic lattice of graphene. A twist angle of $\theta = (1.74^\circ \pm 0.02^\circ)$ was determined from the atomically resolved moiré lattice (42). The red dot indicates the ABBC symmetry position where the spectral maps with applied magnetic field were acquired. Tunneling setpoint $I = 20$ pA; $V_B = 100$ mV; temperature $T = 0.01$ K. (E) Tunneling spectral maps in the D versus V_B plane for $B = 0$ T. n_0 ($-n_0$) indicates the electron density at full filling of the C1 (V1) band. Setpoints: $I = 20$ pA, $V_B = 120$ mV, $T = 0.01$ K. (F) Corresponding theory map for $B = 0$ T (continuum-model calculation). arb. units, arbitrary units.

evolution with displacement field are clearly visible. The experimental data qualitatively agree with the modeled LDOS of the top layer of the four-layer graphene system obtained with continuum-model calculations [Fig. 1F (42)]. The calculations in this work are presented for qualitative comparison and are not meant for quantitative comparison with the experiment.

The trends in the dI/dV map can be qualitatively understood by considering how the theoretically predicted bands in Fig. 1, B and C, fill with n as the Fermi level is raised from negative to positive energies while the bands are modified by the displacement field D . At negative displacement field approaching $D = 0$, the Fermi level is initially pinned to the flat portions of V1 with its associated high LDOS (Fig. 1B). This appears in the spectral maps (Fig. 1, E and F) with the high LDOS of the V1 band located near the Fermi level, corresponding to zero sample bias. Above a displacement field of 0.2 V/nm, the relatively flat C1 band becomes pinned at the Fermi level, and the V1 band develops a larger dispersion while its

highest LDOS at its saddle point moves to lower energies away from C1 with increasing positive displacement field (Fig. 1C). This results in a bright spectral line associated with the saddle point in the V1 band with a negative slope in the top portion of the spectral maps in Fig. 1, E and F.

Mapping Landau levels

Application of a magnetic field creates sharp LLs in the dI/dV spectrum of all four bands, as shown in the dI/dV maps at $B = 4$ T and 8 T in Fig. 2, B and D, respectively (see Figs. S11 to S13 for additional data sets). All dI/dV maps with magnetic field are acquired on an ABBC site (Fig. 1D, red dot). The experimental maps can be compared with the theoretical maps in Fig. 2, C and E, obtained from magnetic field-dependent quantum mechanical calculations (42), following the methods in (44). A series of LL spectra at different displacement fields are extracted from the experimental map at $B = 4$ T (Fig. 2A). The LLs in the V1 band are clearly pronounced and show that the LL energies are irregularly spaced, showing neither the equal spacing char-

acteristic for a parabolic band nor the square root dependence on orbital index as observed in graphene. In the next section, we use the evolution of the V1 LL spacing to experimentally demonstrate the characteristics of the tunable band.

The electron-like versus hole-like character of a band is manifested in the energy variation with LL index and magnetic field B . LLs originating from electron-like Fermi pockets increase in energy with LL index and B , whereas the opposite trend applies for hole-like LLs. The saddle-point energy separates electron-like from hole-like pockets. With this in mind, we examined the experimental spectra of Fig. 2A. At negative displacement field, a set of well-resolved V1 LLs is clearly visible in the dI/dV map at $B = 4$ T (Fig. 2B) and the corresponding extracted spectra (Fig. 2A). We identified the zeroth LL at the bottom of the V1 band, which was at $V_B \approx -45$ mV for zero displacement field. For a given displacement field in Fig. 2A, the LL energy spacing in the V1 band is observed to gradually decrease with increasing bias voltage, followed by a gradual increase,

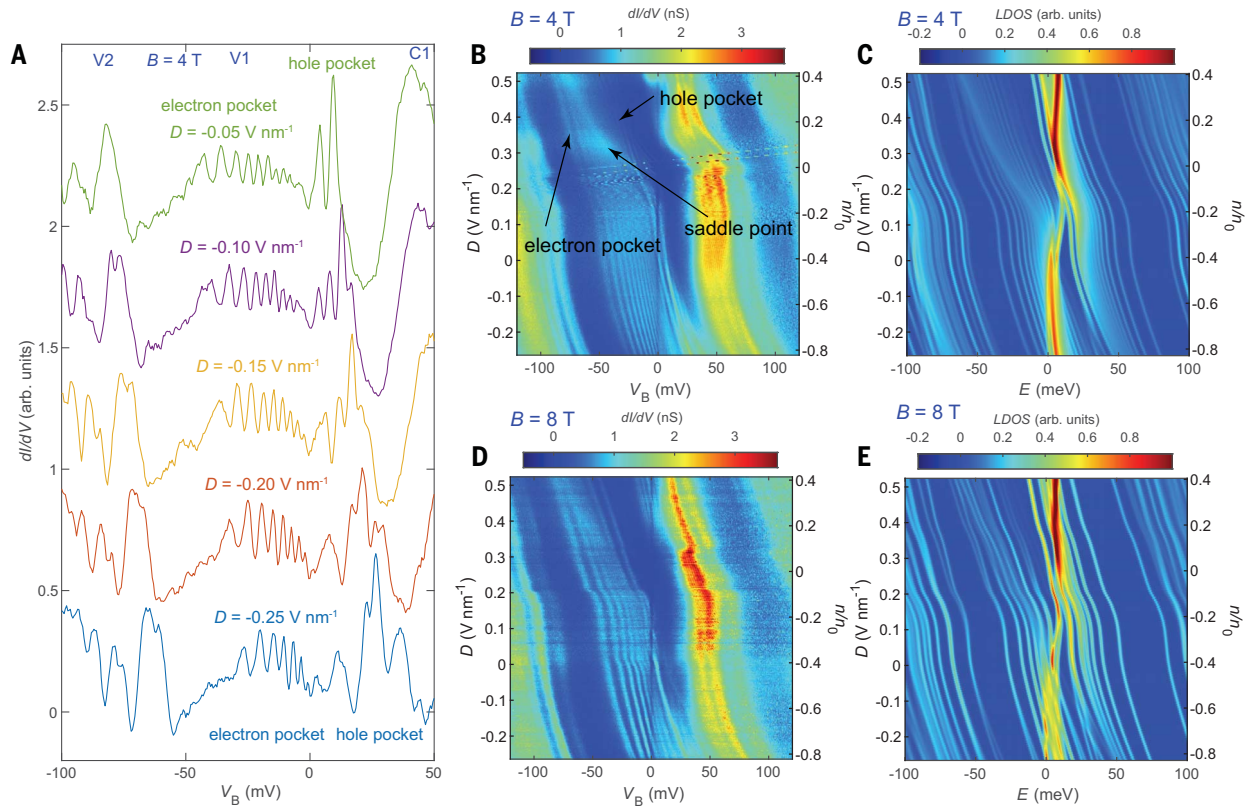


Fig. 2. Tuning LLs in TDBG with displacement and magnetic fields.

(A) Tunneling spectra versus V_B of TDBG at selected displacement fields taken from the map in (B). Tunneling spectral map in the D versus V_B plane at (B) $B = 4$ T. (C) Corresponding theory map for $B = 4$ T (quantum calculation). (D) Tunneling spectral map in the D versus V_B plane at $B = 8$ T.

(E) Corresponding theory map for $B = 8$ T (quantum calculation) (42). The maps in (B) and (D) were acquired on the maxima positions in the moiré structure indicated by the red dot in Fig. 1D. Setpoints: $I = 20$ pA, $V_B = 120$ mV for (B) and (D), $T = 0.01$ K. See Figs. S11 to S13 for additional spectral map data.

pointing to a transition from an electron-like to a hole-like pocket through a saddle point. The LL spacing is inversely proportional to the LDOS, which peaks at the Van Hove singularity at the saddle point. The saddle point is pinned at the Fermi level for negative carrier densities and visible as the high LDOS crossing through the V1 band at positive densities (Fig. 2, B and D).

We used the B -field dependence of the LLs to confirm the nature of the tunable band structure. Figure 3, A to C, displays dI/dV maps in the B versus V_B planes at a fixed displacement field, showing the dispersion of the LLs with B in the V1 band. At negative displacement fields (Fig. 3, B and C), the LLs below the saddle point at the Fermi level disperse with positive slope, and those above the saddle point disperse with negative slope. This confirms the electron versus hole-pocket nature of the V1 band. The transition from electron to hole pocket in the V1 band is similar at positive displacement fields, where increasing displacement fields tunes the V1 saddle point to lower energies (Fig. 3A). At $D = 0.35$ V nm⁻¹ (Fig. 3A), the saddle point is tuned to the middle of the band with an equal number of positive and negative dispersing LLs on either side,

which demonstrates the well-determined tunability of electron and hole pockets with displacement field.

Deviations from the Onsager relation

We now zoom in on the detailed features in the V1 band, leveraging LL spectroscopy to extract quantitative information about the zero-field material properties involving valley-contrasting orbital magnetism and orbital magnetic susceptibility. Figure 3D shows extracted, well-resolved spectra at selected B fields. In Fig. 3E, we show the corresponding peak positions of the LLs in the V1 band versus B for $n = 0$ to 7, which shows how the LLs disperse with magnetic field. LLs are semiclassically described by Onsager's quantization condition, which requires that the total phase accumulation over a cyclotron orbit be an integer multiple of 2π (19). This yields

$$S(E_n)\phi_0/2\pi = 2\pi B_n(n + 1/2) \quad (1)$$

relating the k -space area $S(E_n)$ of the zero-field iso-energy contour of the n th LL E_n to the magnetic field B_n , where $\phi_0 = h/e$ is the magnetic flux quantum, h is Planck's constant,

and e is the elementary charge. With the equal-energy k -space area scaling as $B_n(n + 1/2)$ for all LLs at energy E_n , a plot of $S \propto [B_n(n + 1/2)]_{n=0,1,2,\dots}$ versus LL energy for all LLs would collapse onto a single curve. From Fig. 3E, we plot $S \propto [B_n(n + 1/2)]_{n=0,\dots,7}$ in Fig. 3F. The fact that experimental data points fail to collapse onto a single curve demonstrates the inadequacy of the Onsager relation and the need for higher-order corrections.

Recently, a systematic expansion of the semiclassical Onsager relation described in Eq. 1 was derived by adding corrections in terms of powers of B (21):

$$B_n(n + 1/2)/\phi_0 = S(E_n)/4\pi^2 + m'(E_n)B_n + \chi'(E_n)B_n^2/2 + \dots \quad (2)$$

The coefficients of the first- and second-order correction, $m'(E)$ and $\chi'(E)$, are the derivatives with respect to energy of the total orbital magnetic moment and orbital magnetic susceptibility, respectively. Eq. 2 is thus a powerful tool to either infer the zero-field material properties $S(E)$, $m'(E)$, and $\chi'(E)$ from a given LL spectrum, or to predict the detailed LL spectrum given the knowledge of the zero-field material properties. In the next section, we extract these properties for TDBG from the LL spectrum

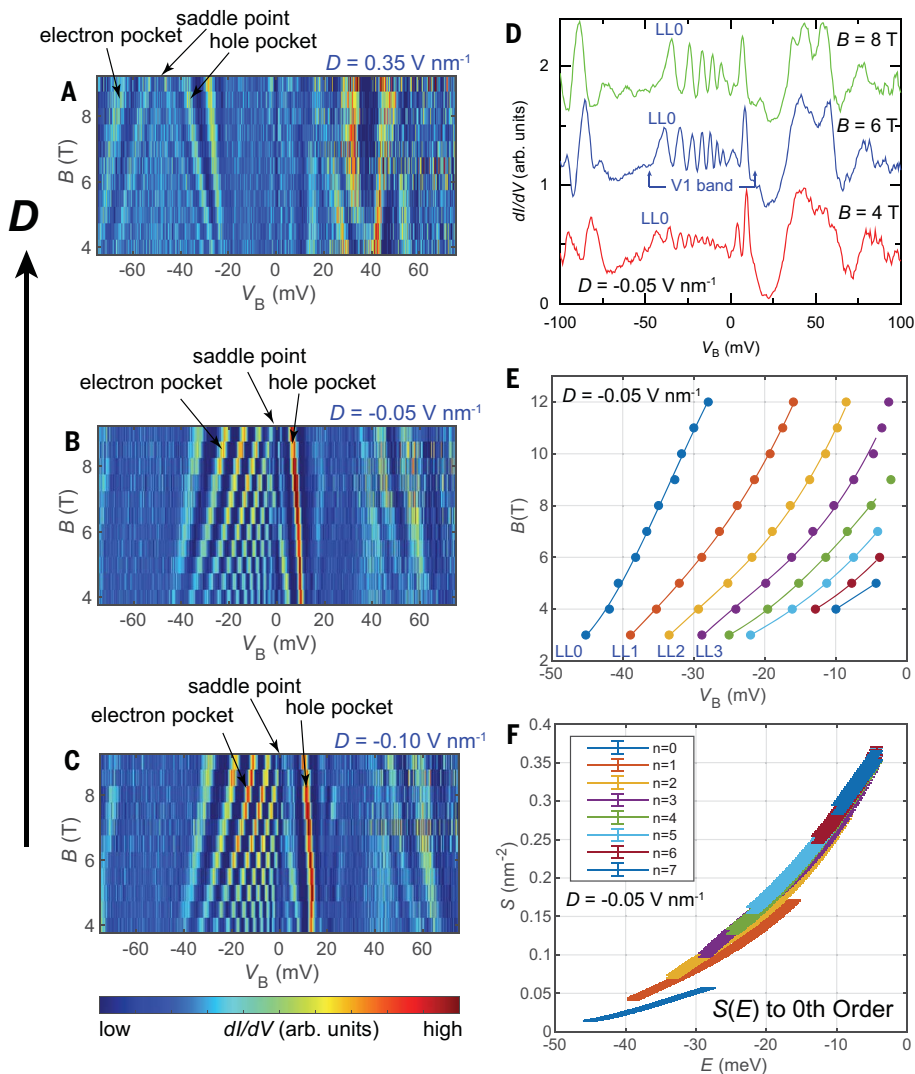


Fig. 3. Breakdown of the standard Onsager relation in TDBG. Spectral maps in the B versus V_B plane for displacement fields of (A) $D = 0.35 \text{ V nm}^{-1}$, (B) $D = -0.05 \text{ V nm}^{-1}$, and (C) $D = -0.1 \text{ V nm}^{-1}$ showing the dispersion of the electron and hole-pocket LLs with magnetic field, and the shift of the V1 saddle point to lower energies with increasing displacement field. (D) Tunneling spectra versus V_B of TDBG as a function of magnetic field at fixed $D = -0.05 \text{ V nm}^{-1}$. (E) LL peak positions versus B for $D = -0.05 \text{ V nm}^{-1}$. Data from LLs $n = 0$ to $n = 8$ are shown. Symbols, experimental peak positions; solid lines, cubic-spline interpolation of experimental peak positions. (F) $S(E)$ computed from the solid lines in (E) with Eq. 1. The lack of data collapse indicates that second-order contributions to the LL energies are substantial.

and show a large contribution of $\chi'(E)$ for moiré systems that scale with an increase in moiré lattice constant.

Extracting zero-field properties

The first-order correction $m'(E)$ includes contributions from the total Berry curvature enclosed by an equal energy contour (Fig. 4, A and B), which yields the well-known Berry phase correction, and the average orbital magnetic moment per carrier at energy E (21, 45). The calculated Berry curvature Ω for the V1 band

is represented by a hue in the mini-Brillouin zone for each valley K and K' in the Brillouin zone in Fig. 4, A and B, respectively. The valleys have equal and opposite Berry curvature and orbital moment. By symmetry, the total intravalley orbital magnetic moment is finite only at nonzero displacement field. This tunability of the valley-contrasting orbital magnetism enables the disentangling of the orbital susceptibility from the orbital magnetic moment, which we use in the analysis of the LLs below. The strength of these contributions in Eq. 2

can be evaluated by using the continuum model. Figure 4C shows the terms on the right side of Eq. 2 for LL0, calculated with the zero-field continuum model and multiplied by ϕ_0/B to obtain the phase contribution in the extended Onsager relation in Eq. 2 (see fig. S5 for all phase contributions). We note that these phase terms are energy dependent and are large in TDBG; for comparison, a value of 0.5 would be equivalent to the π Berry phase in single-layer graphene. The sign of the orbital moment and its derivative $m'(E)$ is opposite for the K and K' valleys, as expected from the valley-contrasting Berry curvature shown in Fig. 4, A and B.

Figure 4D shows how the phase contributions displayed in Fig. 4C drastically alter the semiclassical LL spectrum. The semiclassical, zeroth-order LL spectrum (Eq. 1) is displayed in blue for the lowest LLs in the V1 band by using $S(E)$ obtained from the zero-field continuum model. The first-order correction $m'(E)$ leads to a valley splitting of the LLs indicated by the dashed red and black lines. The calculated valley splitting at the bottom of the V1 band is substantial but within the LL spacing, where the LL index can be assigned unambiguously. This makes LL0 ideally suitable to determine the experimental valley splitting from our high-resolution measurements.

High-resolution dI/dV spectra of LL0 at increasing magnetic fields 9 to 13 T at $D = -0.25 \text{ V/nm}$ are shown in Fig. 4E. We observed a clear experimental splitting, with the red lines indicating the fitted peak positions. At 13 T, the LL0 peak is very broad owing to many levels forming from the Hofstadter spectrum at high magnetic fields. We present a comparison to the spectrum computed quantum mechanically in Fig. 4F (gray peaks) to show the onset of Hofstadter minibands at higher fields. The values of splitting obtained with semiclassical calculations are similar (Fig. 4D). Using an energy broadening comparable to the experiment, shown as the black curve, we obtained qualitative agreement with the experiment. Figure 4G shows a direct comparison of the experimental LL0 splitting in Fig. 4E (blue data points) with the quantum mechanical calculations in Fig. 4F (open orange circles) as a function of B field. We found semiquantitative agreement between the calculated and measured valley-splitting values, demonstrating the tunable valley-contrasting orbital magnetism present in TDBG. Most notably, the splitting was much larger than the standard Zeeman effect with Landé g factor of 2 (solid black line) and did not increase linearly with B field as one would expect for a Zeeman-type splitting mechanism. The latter indicates that the splitting is not only given by $m'(B)$, but rather, a considerable nonzero second-order correction χ' leads to nonlinearity in the splitting with B . We obtained an estimate of m' in the middle of the V1 band of $\approx 3.5 \times 10^{13}$

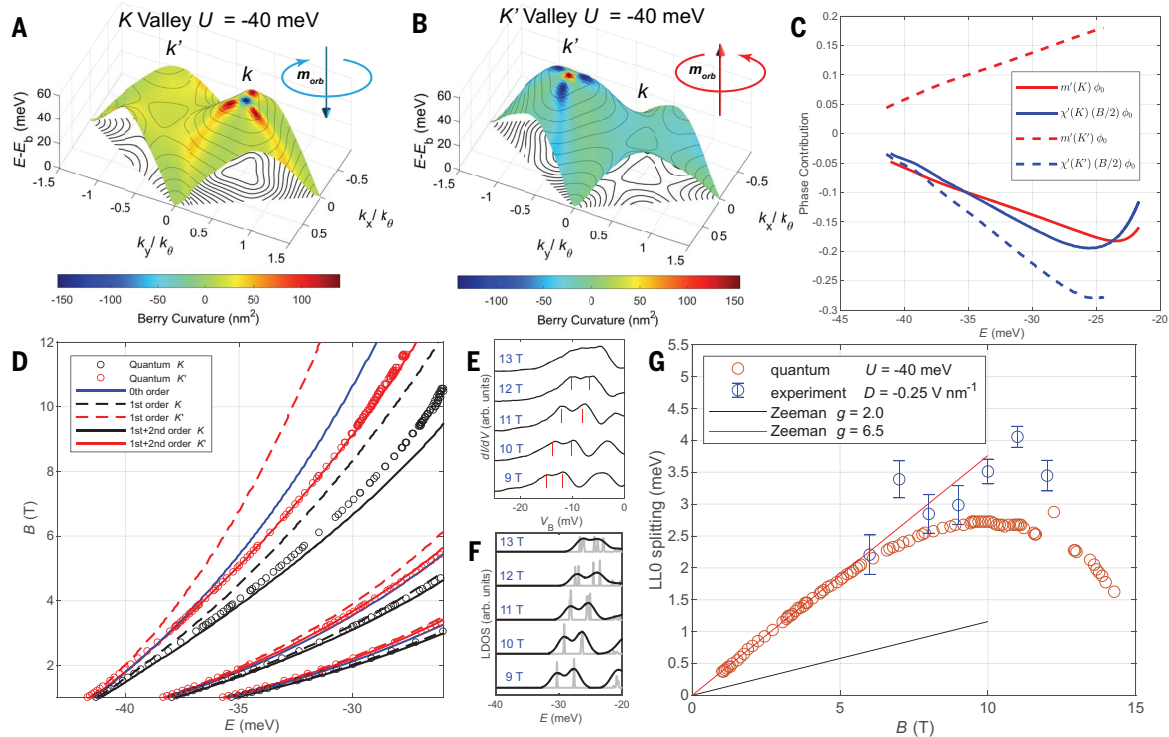


Fig. 4. LL splitting originating from valley-contrasting orbital magnetism and Berry curvature in TDBG. Calculated three-dimensional plot of the V1 band with Berry curvature shading at $U = -40$ meV for (A) K and (B) K' valleys. K and K' valleys have equal and opposite nonzero Berry curvature and equal and opposite orbital magnetic moment (orbital moments depicted schematically). E_b is the D -dependent energy of the bottom of the V1 band. (C) A comparison of the calculated first- (m') and second-order (χ') correction magnitude with the extended Onsager relation for the V1 TDBG band ($U = -40$ meV). See fig. S5 and S6 for additional phase contribution results (42). (D) Calculation of the first few LLs ($n = 0, 1$, and 2) versus B , comparing quantum mechanical to semiclassical methods with zeroth-, first-, and second-order corrections. The first-order correction is grossly deficient in matching the quantum results, particularly in the $n = 0$ level, whereas including both first- and second-order corrections provides a good agreement with the quantum results ($U = -40$ meV). (E) Tunneling spectra of the LLO peak as a

function of B for $D = -0.25$ V nm $^{-1}$ that show a splitting of the LLs in high magnetic fields. The red lines indicate peak positions determined from nonlinear least-square fitting of a double Lorentzian function to LLO. (F) Quantum calculation of LLO as a function of magnetic field for an interlayer potential $U = -40$ meV, corresponding to a displacement field of $D = -0.25$ V nm $^{-1}$. The LL shows a valley splitting upon application of a displacement field. The solid black lines have a Gaussian energy broadening of $\sigma = 1$ meV to match experiment; gray lines, $\sigma = 0.05$ meV. (G) The energy difference of the split $n = 0$ LL from (E) compared with quantum calculations in (F). For the quantum calculation in higher fields, we plot the splitting as the difference in energy between lowest levels in the Hofstadter bands of the K and K' valleys. The uncertainty in the experimental points is derived from twice the standard deviation obtained from the nonlinear least-square fits of the peaks in (E). For comparison, the solid lines show the calculated Zeeman splitting with Landé g factor of (black) $g = 2$ and (red) 6.5.

C/(J s), comparable to a calculated estimate of $\approx 4.4 \times 10^{13}$ C/(J s), using the values for the splitting, $S(E)$ and $\chi'(E)$, extracted from the experiment (42).

The first-order correction m' does not explain the lack of collapse of the LLs onto a single curve. This is the result of a strong, experimentally observable second-order correction, given by the energy-dependent orbital magnetic susceptibility $\chi'(E)$. This contribution originates from several mechanisms, as elucidated in recent theoretical works (18, 46, 47), including the geometrical origin, namely the Berry curvature and quantum metric (48). The calculated $\chi'(E)$ of TDBG has the same sign for both the K and K' valley, as shown for LLO in Fig. 4C. This results in a shift of the valley-split LLs, quadratically increasing with B field, as shown by the black and red solid lines in the continuum-model calculation in Fig. 4D. This fully expanded semiclassical approximation with first- and second-order correction

(Eq. 2) agrees well with the quantum mechanical spectrum obtained for the same system (red and black open circles), again emphasizing the importance of the second-order correction to adequately describe the system. For a large region of energies and magnetic fields, the second-order correction is larger than the first one (Fig. 4, C and D, and fig. S6). This means that the energy-dependence of the magnetic field-induced orbital moment exceeds the displacement field-induced orbital moment.

To extract the second-order correction to the LL energy, we note that the first-order splitting is typically not visually evident for most electron-like LLs in the V1 band at smaller displacement fields owing to smaller valley splitting from orbital magnetism, and presumably, to broadening. The energy value of a single LL peak is then approximately the average of the valley-split values. The valley-averaged energy at a fixed displacement field

is obtained from Eq. 2 by letting $m'(E) = 0$, keeping only the second-order correction. For equal energy LLs n and m with associated fields B_n and B_m , Eq. 2 yields the following for S and χ' :

$$S(E) = \frac{2\pi e}{h} B_n B_m \left[\frac{B_m(n+1/2) - B_n(m+1/2)}{(B_m^2 - B_n^2)} \right] \quad (3)$$

$$\chi'(E) = \frac{e}{\pi h} \left[\frac{B_n(n+1/2) - B_m(m+1/2)}{(B_n^2 - B_m^2)} \right] \quad (4)$$

Figure 5A shows the average values of $S(E)$ obtained by evaluating Eq. 3 for all pairs of LLs in Fig. 3E at each energy value. By contrast to Fig. 3F, $S(E)$ collapses onto a single curve (blue data points) in Fig. 5A, confirming the

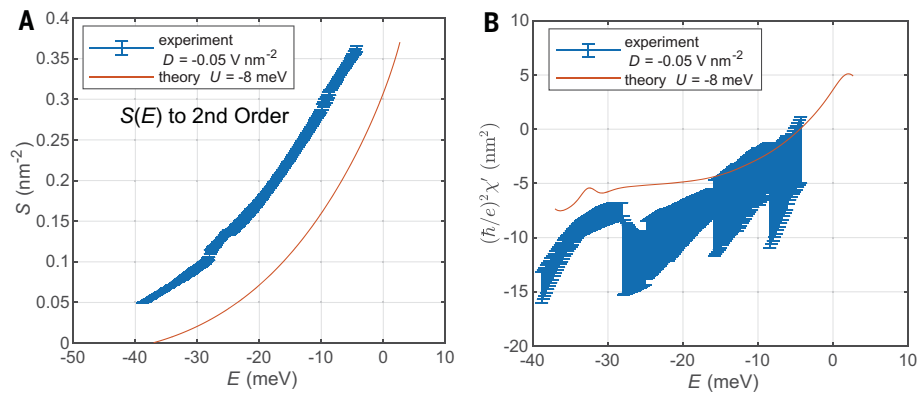


Fig. 5. Extraction of enhanced energy-dependent orbital magnetic susceptibility in moiré quantum matter from the extended Onsager relation. (A) The symbols represent $S(E)$ computed from the solid lines in Fig. 3E with Eq. 3, demonstrating data collapse onto one continuous curve. The solid line represents $S(E)$ computed for the V1 band from continuum-model calculations. (B) The symbols represent $\chi'(E)$ computed from the solid lines in Fig. 3E with Eq. 4. The solid line represents $\chi'(E)$ computed from continuum-model calculations. See (42) for a discussion of the error analysis.

applicability of the second-order correction. The result has a similar trend to that of the zero-field continuum-model calculation of $S(E)$ (orange solid line).

Similarly, we obtained the average value of $\chi'(E)$ by evaluating Eq. 4 (blue data points in Fig. 5B). The experimentally extracted values are in qualitative agreement with the zero-field orbital magnetic susceptibility (orange line), computed with the continuum model according to the formalism of (49). The uncertainty in the extracted $\chi'(E)$ and the deviation in overlap of segments from different pairs of LLs are attributed to two factors. First, corrections to Landau quantization energies have a smaller impact on the high-index LLs located at higher energies (50). Extracting the relatively smaller corrections at these energies therefore leads to larger uncertainty. Second, variations of the chemical potential with magnetic field shift the LL energy positions, especially at high magnetic fields (42). We do not believe interactions make a qualitative impact on our analysis. The LL scaling obtained with the extended Onsager relation is highly constrained, and we find it is well satisfied over a wide range of electron filling. Presumably, interactions would renormalize LL energies in a distinct manner, which would depend strongly on filling factor.

Discussion and outlook

There are several distinct microscopic mechanisms that underlie the orbital magnetic susceptibility, including recently identified geometric contributions (18, 46). In fig. S9, we show the contributions to $\chi'(E)$ from these mechanisms [see (42) for the full breakdown]. The contributions from the Pauli paramagnetism and the quantum geometry involve the orbital magnetic moment, Berry curvature, and quantum

metric. These mechanisms make the dominant contribution to $\chi'(E)$ near the top of V1 and bottom of C1 bands, where the Berry curvature is peaked (Fig. 4, A and B). The contributions from the van Vleck paramagnetism and k -space energy polarization are dominant in the middle of the V1 band, whereas the well-known Landau-Peierls susceptibility is substantial at the band edges.

We attribute the large value of $\chi'(E)$ to the large lattice constant a of the moiré potential. This can be roughly understood with dimensional analysis: for a single band model, the total orbital magnetic susceptibility χ generally scales as Wa^2 , where W is the bandwidth, so that the derivative of χ with respect to energy then scales as a^2 , which can be large for moiré quantum systems. For a more in-depth analysis, see fig. S10, A and B, which shows that the maximum value of χ' increases dramatically with increasing moiré wavelength, indicating that future measurements of orbital magnetism should be even more observable at larger wavelengths.

MQM holds great opportunities for efficient magnetization control, topological transport phenomena, the quantum anomalous Hall effect, and technological applications in magnetoelectric, magneto-optics, and topological spintronics. Understanding the underlying band topology and magnetic response functions are the key metrological capability required to practically harness all these opportunities. Our measurements and analysis point a way forward to this goal.

REFERENCES AND NOTES

1. National Academies of Sciences, Engineering, and Medicine, *Theoretical Considerations Concerning Moiré Quantum Materials in Frontiers in Synthetic Moiré Quantum Matter: Proceedings of a Workshop* (2022); <https://nap.nationalacademies.org/catalog/26594/>

- frontiers-in-synthetic-moire-quantum-matter-proceedings-of-a-workshop.
2. D. M. Kennes et al., *Nat. Phys.* **17**, 155–163 (2021).
3. R. Bistritzer, A. H. MacDonald, *Proc. Natl. Acad. Sci. U.S.A.* **108**, 12233–12237 (2011).
4. Y. Cao et al., *Nature* **556**, 80–84 (2018).
5. Y. Cao et al., *Nature* **556**, 43–50 (2018).
6. J. M. Park, Y. Cao, K. Watanabe, T. Taniguchi, P. Jarillo-Herrero, *Nature* **590**, 249–255 (2021).
7. Y. Cao, J. M. Park, K. Watanabe, T. Taniguchi, P. Jarillo-Herrero, *Nature* **595**, 526–531 (2021).
8. H. Zhou, T. Xie, T. Taniguchi, K. Watanabe, A. F. Young, *Nature* **598**, 434–438 (2021).
9. J. M. Park et al., *Nat. Mater.* **21**, 877–883 (2022).
10. G. W. Burg et al., *Nat. Mater.* **21**, 884–889 (2022).
11. Y. Zhang et al., *Science* **377**, 1538–1543 (2022).
12. Y.-H. Zhang, D. Mao, Y. Cao, P. Jarillo-Herrero, T. Senthil, *Phys. Rev. B* **99**, 075127 (2019).
13. M. V. Berry, *Proc. Royal Soc., Math. Phys. Eng. Sci.* **392**, 45–57 (1984).
14. A. L. Sharpe et al., *Science* **365**, 605–608 (2019).
15. M. Serlin et al., *Science* **367**, 900–903 (2020).
16. S. Sinha et al., *Nat. Commun.* **11**, 5548 (2020).
17. D. Xiao, M.-C. Chang, Q. Niu, *Rev. Mod. Phys.* **82**, 1959–2007 (2010).
18. Y. Gao, S. A. Yang, Q. Niu, *Phys. Rev. B Condens. Matter Mater. Phys.* **91**, 214405 (2015).
19. L. Onsager, *Lond. Edinb. Dublin Philos. Mag. J. Sci.* **43**, 1006–1008 (1952).
20. L. M. Roth, *Phys. Rev.* **145**, 434–448 (1966).
21. Y. Gao, Q. Niu, *Proc. Natl. Acad. Sci. U.S.A.* **114**, 7295–7300 (2017).
22. C. Shen et al., *Nat. Phys.* **16**, 520–525 (2020).
23. X. Liu et al., *Nature* **583**, 221–225 (2020).
24. M. He et al., *Nat. Phys.* **17**, 26–30 (2021).
25. Y. Cao et al., *Nature* **583**, 215–220 (2020).
26. P. C. Adak et al., *Phys. Rev. B* **101**, 125428 (2020).
27. S. Sinha et al., *Nat. Phys.* **18**, 765–770 (2022).
28. C. Zhang et al., *Nat. Commun.* **12**, 2516 (2021).
29. X. Liu et al., *Nat. Commun.* **12**, 2732 (2021).
30. C. Rubio-Verdú et al., *Nat. Phys.* **18**, 196–202 (2021).
31. P. Rickhaus et al., *Science* **373**, 1257–1260 (2021).
32. J. Y. Lee et al., *Nat. Commun.* **10**, 5333 (2019).
33. M. Koshino, *Phys. Rev. B* **99**, 235406 (2019).
34. N. R. Chebrolu, B. L. Chittari, J. Jung, *Phys. Rev. B* **99**, 235417 (2019).
35. Y. W. Choi, H. J. Choi, *Phys. Rev. B* **100**, 201402 (2019).
36. F. J. Culchac, R. R. Del Grande, R. B. Capaz, L. Chico, E. S. Morell, *Nanoscale* **12**, 5014–5020 (2020).
37. F. Haddadi, Q. Wu, A. J. Kruchkov, O. V. Yazyev, *Nano Lett.* **20**, 2410–2415 (2020).
38. J. A. Crosse, N. Nakatsuji, M. Koshino, P. Moon, *Phys. Rev. B* **102**, 035421 (2020).
39. M. Kuiri et al., *Nat. Commun.* **13**, 6468 (2022).
40. Y. J. Song et al., *Rev. Sci. Instrum.* **81**, 121101 (2010).
41. J. Schwenk et al., *Rev. Sci. Instrum.* **91**, 071101 (2020).
42. Additional supplementary text and data are available in the supplementary materials.
43. J. A. Stroscio, W. J. Kaiser, *Scanning Tunneling Microscopy: Volume 27 (Methods of Experimental Physics)* (Academic Press, 1993).
44. R. Bistritzer, A. H. MacDonald, *Phys. Rev. B Condens. Matter Mater. Phys.* **84**, 035440 (2011).
45. M.-C. Chang, Q. Niu, *J. Phys. Condens. Matter* **20**, 193202 (2008).
46. F. Piéchon, A. Raoux, J.-N. Fuchs, G. Montambaux, *Phys. Rev. B* **94**, 134423 (2016).
47. M. Ogata, H. Fukuyama, *J. Phys. Soc. Jpn.* **84**, 124708 (2015).
48. F. Wilczek, A. Shapere, *Geometric Phases in Physics in Advanced Series in Mathematical Physics* (World Scientific, 1989), vol. 5; <https://www.worldscientific.com/worldscibooks/10.1142/0613>.
49. H. Fukuyama, *Prog. Theor. Phys.* **45**, 704–729 (1971).
50. J.-N. Fuchs, F. Piéchon, G. Montambaux, *SciPost Physics* **4**, 024 (2018).
51. M. R. Slot et al., Replication Data for A Quantum Ruler for Orbital Magnetism in Moiré Quantum Matter, George Mason University Dataverse (2023); <https://doi.org/10.13021/orc2020/RLZTDF>.

ACKNOWLEDGMENTS

We thank F. J. Giessibl for providing the qPlus AFM sensors and general advice on AFM measurements. **Funding:** University of Maryland and the National Institute of Standards and Technology (NIST) PREP program grant no. 70NANB18H165 (Y.M., E.M.S., and E.S.); Georgetown University and NIST PREP program grant no. 70NANB18H161 (M.R.S.); University of Maryland and NIST Joint Quantum Institute grant no. 70NANB21H126 (S.K. and D.Y.); Office of Naval Research grant no. N00014-20-1-2352 (S.K. and D.Y.); Japan Society for the Promotion of Science KAKENHI grant nos. 19H05790, 20H00354, and 21H05233 (T.T. and K.W.); Dutch Research Council (NWO) through Rubicon grant no. 019.193EN.026 (M.R.S.); University of Reno start-up grant no. PG19012 (Y.B.). **Author contributions:** Conceptualization: F.G.,

P.M.H., J.A.S., and N.B.Z.; Methodology: P.M.H. and Y.B.; Investigation: M.R.S., Y.M., S.K., D.T.W., E.S., S.T.L., E.M.S., D.Y., S.R.B., and F.G.; Visualization: Y.M., M.R.S., P.M.H., and J.A.S.; Project administration: J.A.S.; Supervision: J.A.S. and N.B.Z.; Resources: K.W. and T.T.; Software: P.M.H., Y.B., M.R.S., Y.M., S.K., D.T.W., and J.A.S.; Writing – original draft: M.R.S., Y.M., P.M.H., N.B.Z., F.G., and J.A.S.; Writing – review and editing: M.R.S., Y.M., P.M.H., S.K., D.T.W., E.S., S.T.L., E.M.S., D.Y., S.R.B., K.W., T.T., T.B., N.B.Z., F.G., and J.A.S. **Competing interests:** The authors declare that they have no competing interests. **Data and materials availability:** The data from this study and the code used to generate theoretical results in this study are available at the George Mason University Dataverse (51). **License information:** Copyright © 2023 the authors, some rights reserved; exclusive

licensee American Association for the Advancement of Science. No claim to original US government works. <https://www.science.org/about/science-licenses-journal-article-reuse>

SUPPLEMENTARY MATERIALS

science.org/doi/10.1126/science.adf2040
Materials and Methods
Supplementary Text
Figs. S1 to S13
References (52–56)

Submitted 5 October 2022; resubmitted 1 March 2023
Accepted 30 August 2023
[10.1126/science.adf2040](https://doi.org/10.1126/science.adf2040)